Comprehensive Model of Laminar Jamming Variable Stiffness Driven by Electrostatic Adhesion

Cheng Chen, Dongliang Fan, Hongliang Ren, *Senior Member, IEEE*, and Hongqiang Wang, *Senior Member, IEEE*

***Abstract*—Variable stiffness mechanisms empower robots to become compliant or rigid on demand for adapting to challenging scenarios, such as gripping irregular fragile objects without damaging them or exploring complicated environments, i.e., natural channels inside human bodies, safely. However, variable stiffness mechanisms are typically constrained by bulky structures, slow actuation, low stiffness variation, and especially the lack of nonlinear behaviors modeling. We aim to build an explicit analytical model to characterize nonlinear behaviors of the laminar jamming variable stiffness mechanism. In this work, we demonstrate a low-cost (<0.08 USD for each layer), lightweight (0.5 g each layer), compact (85 μm thick each layer), and scalable (arbitrary dimensions of electrodes) laminar jamming structure based on electrostatic adhesion. The analytical model that explains thorough mechanical behaviors of a two-layer structure, including linear (constant stiffness) and nonlinear (stiffness varies) regimes, is developed, showing high accuracy with experimental results under different driving voltages. Based on the model, the influences of parameters such as material properties, geometry, and voltages on the stiffness performance are analyzed, giving potential improvement directions in materials, design, and actuation. The mechanical behaviors of two-layer and four-layer structures are characterized through three-point bending tests. The performances, including the stiffness variation (4 layers, up to 11 times), responding time (700–800 ms), and power consumption (1 mW), are also evaluated experimentally. We demonstrate the response speed, the impact absorption functionality, and the deflection prediction. The design, fabrication, and modeling herein pave the way for developing multifunctional robots with variable stiffness.**

***Index Terms*—Electrostatic adhesion, laminar jamming, variable stiffness.**

Manuscript received 22 November 2022; revised 8 June 2023; accepted 12 September 2023. Recommended by Technical Editor H. Yu and Senior Editor N. G. Tsagarakis. This work was supported in part by the National Natural Science Foundation of China under Grant 52275021, in part by the National Key R&D Program of China under Grant 2022YFB4701200, in part by the Shenzhen Science and Technology Innovation Commission under Grant ZDSYS20220527171403009, in part by the Science, Technology, and Innovation Commission of Shenzhen Municipality under Grant ZDSYS20200811143601004, in part by the Southern Marine Science and Engineering Guangdong Laboratory (Guangzhou) under Grant K19313901, in part by the Regional Joint Fund Project of the Basic and Applied Research Fund of Guangdong Province though Project 2021B1515120035 under Grant B.02.21.00101, and in part by Hong Kong Research Grants Council Collaborative Research Fund under Grant C4026-21G. *(Corresponding authors: Hongliang Ren; Hongqiang Wang.)*

Cheng Chen is with the Shenzhen Key Laboratory of Intelligent Robotics and Flexible Manufacturing Systems, Southern University of Science and Technology, Shenzhen 518055, China, and also with the Department of Biomedical Engineering, National University of Singapore, Singapore 117575 (e-mail: cheng.ch97@gmail.com).

Dongliang Fan is with the Shenzhen Key Laboratory of Intelligent Robotics and Flexible Manufacturing Systems, Southern University of Science and Technology, Shenzhen 518055, China (e-mail: dlfan0902@gmail.com).

Hongliang Ren is with the Department of Biomedical Engineering, National University of Singapore, Singapore 117575, and also with the Department of Electronic Engineering, Shun Hing Institute of Advanced Engineering, The Chinese University of Hong Kong, Hong Kong (e-mail: ren@nus.edu.sg).

Hongqiang Wang is with the Shenzhen Key Laboratory of Intelligent Robotics and Flexible Manufacturing Systems, Southern University of Science and Technology, Shenzhen 518055, China, also with the Guangdong Provincial Key Laboratory of Human-Augmentation and Rehabilitation Robotics in Universities, Southern University of Science and Technology, Shenzhen 518055, China, and also with the Southern Marine Science and Engineering Guangdong Laboratory, Guangzhou 510000, China (e-mail: wanghq6@sustech.edu.cn).

This article has supplementary material provided by the authors and color versions of one or more figures available at https://doi.org/10.1109/TMECH.2023.3319650.

Digital Object Identifier 10.1109/TMECH.2023.3319650

I. Introduction

In DECADES, multiple bioinspired soft robots, whether in materials, actuation, or design, have been developed [1], [2]. Soft robots are highly compliant and robust to external impact by benefitting from elastic and flexible materials. They can adaptively interact with complex scenarios, such as water surface [3] and deep sea [4]. However, unlike traditional rigid robots, soft robots can barely output high force/torque, lock shape, and resist external forces simultaneously. To enhance the functionality and expand the application boundaries of soft robotics, controllable variable stiffness technology is the key technique. Variable stiffness technology bridges the gap between soft robots and rigid robots and transforms among different stiffnesses on demand, satisfying various application needs, or environments upon request. For instance, a soft modular manipulator [7] can interact with surrounding biological structures and carry out surgical tasks simultaneously through selective stiffening, allowing the proximal part to hold organs and the remaining portion to perform grasping.

Previously various mechanisms and structures have been proposed for variable stiffness, such as structural antagonism, granular jamming, and laminar jamming. Inspired by soft animals, structural antagonism is implemented by the actuators that generate forces or torques in opposite directions [5], [6]. Granular jamming is typically composed of granular materials sealed in a chamber. By adjusting the vacuum gradient inside the chamber to alter the density of encapsulated granular materials, the particles can present solid, or fluid physical properties [7], [8], [9]. A granular jamming-based manipulator modular with 2.3 times the stiffness ratio (high stiffness/low stiffness) was proposed [7]. Laminar jamming, which is usually composed of multiple stacked layers, is acknowledged as a promising technique because of its compact and lightweight structure and large stiffness ratio [10], [11], [12]. The stiffness rises by increasing the friction force (jamming) between layers. The stiffness variation is determined by the moment of inertia of the structure, which is regulated by the interlayer jamming and the number of jamming layers. For example, by utilizing shape memory alloys (SMA) wires to wrap around ten polycarbonate layers [10], the maximum stiffness change reaches 60 times through selective stiffening. When an encapsulated multilayer paper structure is under different vacuum gradients, the longitudinal load it withstands changes intensely. The stiffness ratio is up to 6.65 times in the previous work [12]. However, the actuation for these variable stiffness mechanisms is usually challenging. Whether fluid-driven or vacuum-driven, high-power external sources bring both driving methods significant challenges to portability, working noise, and energy consumption. The temperature-driven method, such as SMA [10], needs a long recovery time due to poor heat dissipation conditions.

In recent years, the electrostatic-driven technique has thrived because of its superiorities, e.g., quiet working conditions, low energy consumption, fast response, and high force density. Many excellent works have been reported by utilizing this technique to endow robots with new functions, such as motors and actuators [13], [14], climbing and flying robots [15], [16], [17], [18], clutches [19], [20], [21], [22] for human rehabilitation and enhancement, and artificial muscles for surgery tasks [23]. This technique was not applied to variable stiffness until an electrostatic adhesion based laminar jamming structure was reported [24]. Tests were conducted to evaluate the structure's tensile stiffness and bending stiffness. However, there was a significant discrepancy between the experimental results and the electrostatic modeling. Moreover, the previous model cannot explain the nonlinear behavior with the increase of the force when the deflection is large. Since nonlinear behaviors are common and almost inevitable for variable stiffness devices that are applied by unknown and changing external loads, more comprehensive nonlinear modeling is desired to explain and predict its mechanical behavior for further precise control and practical applications of this technique.

Experiments [5], [6], [7] and/or simulations [8], [9], [10] are commonly used to characterize the examined variable stiffness devices via structural antagonism and granular jamming within this article's research scope. For laminar jamming, three-point bending tests were conducted for a multilayer structure and validated with FEM, and an algebraically taxing model was built but failed to predict the deflection [12]. An analytical model of laminar jamming was proposed and validated with FEM [32]. However, the linear mechanical model was applied to characterize the nonlinear mechanical behavior, which might explain the discrepancy between FEM and theory. Both models are only valid for small deflections; the latter is smaller than 1.5 mm. In this article, we first develop a nonlinear analytical model that comprehensively explains the variable stiffness mechanism based on beam theory and the idea of neutral axes separation [26], [27], [28]. We mathematically describe the mechanical process of bending an electrostatic laminar jamming structure (ELJS) containing multiple electrode films from small to large deflection (up to 4 mm). This model is validated through experimental results. The parametrical analysis is given based on this model, presenting how to improve the stiffness-related performances that critically depend on the design inputs (e.g., materials, geometry, and voltages). A lightweight (0.5 g each layer) and compact (85 μm thick each layer) multilayer ELJS is fabricated. Then three-point bending tests are conducted to characterize the mechanical behaviors of a two-layer and a four-layer ELJS, presenting a maximum stiffness variation of 11 times. Experimental results also exhibit a fast response (700–800 ms) and low power consumption of ELJS (only 1 mW). At last, a two-layer and a six-layer ELJS with different dimensions are fabricated to exhibit fast response speed, impact absorption ability for protecting fragile objects, and accurate deflection prediction for possible medical applications.

II. Modeling and Fabrication

A. Electrostatic Adhesion

A typical ELJS is made of two identical electrode films. Each electrode film is composited by an electrode and a dielectric layer. The two-layer ELJS is an ideal parallel-plate capacitor [see Fig. 1(a)]. When a voltage is applied to electrodes, an electric field is generated, bringing the electrostatic adhesion force

$$F_{EA} = \frac{\varepsilon_0 \varepsilon_r S}{2} \left(\frac{U}{d} \right)^2 \tag{1}$$

where ε_0, ε_r, U, d, and S are the vacuum permittivity constant, the relative permittivity of dielectric, applied voltage on electrodes, the thickness of the dielectric layer if not considering air gaps, and the effective adhesion area, respectively. In this work, the effective adhesion area $S = Lb$, where L and b are the length and width of an electrode, respectively, and t is the electrode thickness [see Fig. 1(a)]. As shown at the right of Fig. 1(b), electrostatic adhesion force transforms the loosely stacked electrode films to a firmly coupling state, thus stiffening in structure. More specifically, when an external pressing load is applied to the ELJS span, the shear stress tends to develop relative sliding between electrode films. However, the friction force along the longitudinal interface prevents this movement occurrence, therefore maintaining the structure in the jamming

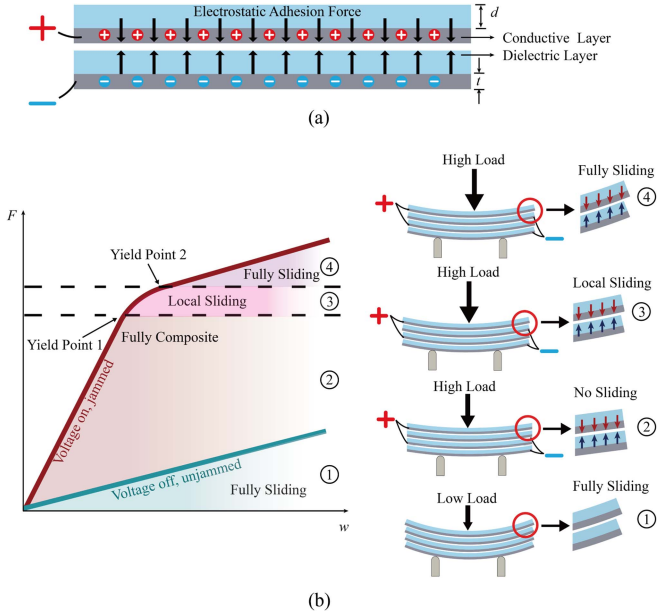

Fig. 1. Schematic diagram of the electrostatic laminar jamming structure (ELJS) model. (a) Two-layer ELJS. Each electrode film contains an electrode and a dielectric layer. (b) Mechanical behaviors of a multilayer ELJS under three-point bending test. Three regimes, fully composite, local sliding, and fully sliding between electrode films, chronologically happen.

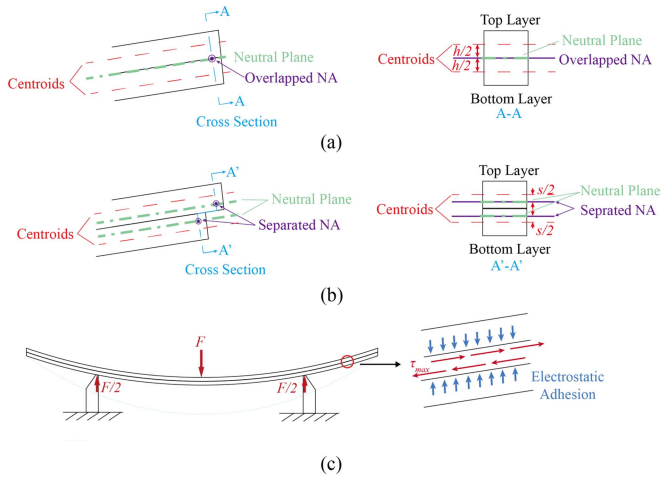

Fig. 2. Two-layer ELJS in its (a) fully composite mode, where the neutral axes (NAs) of electrode films remain overlapped at the cross-sectional interface, and (b) in local sliding mode, where the NA of each layer decouples and separates from the overlapped position. (c) Force diagram of a two-layer ELJS.

state. The maximum static friction force provided by electrostatic adhesion force can be expressed as

$$f_s = \mu F_{EA} \tag{2}$$

where μ is the coefficient of friction between two electrode films.

B. Variable Stiffness

The stiffness of a beam is expressed as

$$k = \frac{F}{w} = \frac{48EI}{l^3} \tag{3}$$

where F and w are the external concentrated pressing load applied at the midspan, and the corresponding deflection, respectively; E, I, and l are plane strain modulus, the moment of inertia, and the distance between fixtures, respectively. The boundary conditions of the simply supported beam and concentrated load at midspan are applied here. Other conditions can also be applied accordingly based on beam theory. When the electrode films are loosely stacked together (no voltage applied), the moment of inertia equals the sum of the moment of inertia of each electrode film

$$I_U = nI_u = n\frac{bh^3}{12} \tag{4}$$

where n is the number of layers of electrode film, and I_u and h are the moment of inertia in form of rectangular cross section and the thickness of each electrode film, respectively. Once the voltage is applied, the structure is transformed by electrostatic adhesion force into a fully composite beam with a thickness of nh

$$I_J = n^3\frac{bh^3}{12}. \tag{5}$$

According to (4) and (5), the stiffness ratio is obtained by

$$r = \frac{k_J}{k_U} = \frac{EI_J}{EI_U} = n^2 \tag{6}$$

inferring that the stiffness variation is proportional to the square of the number of layers. For instance, the stiffness in the jammed state is four times larger than that in the unjammed state for a two-layer ELJS and 100 times larger for a ten-layer ELJS.

The abovementioned equations have been employed to explain the stiffness variation of layer jamming in previous literature [10], [11], [12]. According to (3), the concentrated loading force linearly increases with the deflection. This relationship remains effective at the beginning of the bending but becomes inapplicable when the force-deflection curvature enters a nonlinear zone, where the interlayer slip first occurs. The nonlinear increase of the force results from the local sliding between electrode layers, while the abovementioned equations hypothesize the layers are fully composite. To explain all the processes of stiffness variance, here we introduce a more general equation [25] between EI_J and EI_U, in, e.g., the two-layer jamming situation

$$EI_J = EI_U + \frac{EA_p s^2}{EA_0} \tag{7}$$

where $EA_p = EA_1 \cdot EA_2$, and $EA_0 = EA_1 + EA_2$. s is the distance between the neutral axes (NAs) and the centroids of the two layers, as shown in Fig. 2(b). EA_1, EA_2, and EA_0 are axial stiffness of the top and bottom layers, and the sum of axial stiffness of two layers, respectively. Both the axial stiffness and the first-order derivative of the internal normal force, which equals the internal shear force per length for a differential element, partially contribute to the interlayer sliding.

And EA_p is the product of the axial stiffness of each layer. For a more comprehensive equation of an n-layer ELJS, the similar relation of the ith and $(i+1)$th layer is derived as

$$EI_{J(i,i+1)} = \sum_{i}^{i+1} EI_{U(i)} + \frac{s_i^2}{\sum_i^{i+1} EA_i}. \tag{8}$$

Hence, the stiffness of an arbitrary layer i can be obtained by solving each NA separation movement. Here, the classic two-layered ELJS with cathode-anode staggered arrangements is discussed.

According to the relative motion between two layers, we define the status into three modes: 1) fully composite, 2) local sliding, and 3) fully sliding, as shown in Fig. 1(b). In the fully composite mode, layers are fully jammed with no relative sliding so that ELJS can be regarded as a whole solid beam. Therefore, the NAs of the two layers remain overlapped at the cross-sectional interface [see Fig. 2(a)]. Based on beam theory, the maximum shear stress [see Fig. 2(c)] happens along with the longitudinal interface for three-point bending

$$\tau_{\max} = \frac{3F}{4A} \tag{9}$$

where $A = nbh$ is the cross-sectional area of a multilayer ELJS. For ELJS with even layers, the longitudinal interface is the contact interface between layers. The maximum shear stress from the concentrated load increases and drives the sliding tendency between layers, but ELJS remains fully composite before the stress overcomes the maximum static friction force f_s caused by the electrostatic adhesion force between layers

$$\tau_{\max} = \frac{3F_{c1}}{4nbh} = \frac{f_s}{S} \tag{10}$$

where F_{c1} is the external pressing load at yield point 1, as shown at the left of Fig. 1(b). After yield point 1, the beam structure is no longer fully composite but emerges with interlayer relative sliding displacement due to bending radius discontinuities at both ends of layers, as shown at the left of Fig. 2(b). More precisely, the layers of ELJS become less coupled and more independent from each other; thus, the NA of each layer also becomes independent and begins to separate from each other, as shown at the right of Fig. 2(b). The separated NAs approach the centroids of the corresponding layers independently as load F increases along with the deflection w. According to (7), as the NAs approach the centroids till the variable s reaches its minimum value, the fully sliding mode takes place. This directly causes the stiffness decrement because layers in the fully sliding regime are similar to that under the unjammed state, in which each layer is considered an independent beam whose NA coincides with its centroid.

Assuming NAs follow the same trajectory in the local sliding regime, then we only need to analyze the NA movement of the top half. Equation (7) can be rewritten as

$$\frac{EI}{EI_U} = 1 + 3\mathrm{NA}(w)^2 \tag{11}$$

where

$$\mathrm{NA}(w) = \begin{cases} 1, F \le F_{c1} \\ \frac{s/2}{h/2}, F > F_{c1} \end{cases} \tag{12}$$

is the normalized NA movement distance. (11) shows the impact of NA movement on ELJ stiffness. By replacing EI in (3) with $EI_U[1 + 3NA(w)^2]$, the governing equation is derived

$$F = \frac{48EI_U}{l^3} w \left[1 + 3\mathrm{NA}(w)^2\right]. \tag{13}$$

The stiffness is defined as the slope of $F(w)$

$$k = \frac{\partial F}{\partial w}. \tag{14}$$

As illustrated in Fig. 1(b), the starting point (yield point 1) and the endpoint (yield point 2) of the local sliding regime should be continuous in force and stiffness

$$\begin{cases} F(w_1) = k_J w_1 \\ F(w_2) = F_{c2} \\ k(w_1) = k_J \\ k(w_2) = b_2 k_U \end{cases}. \tag{15}$$

ELJS, either in a jammed or unjammed state, develops to the full sliding regime during the three-point bending. Hence, the form of work done by the external pressing load in the local sliding regime, which represents the transition of ELJS from fully composite to fully sliding, should equal that in the corresponding regime of the unjammed state where the bending radius is the same as that of the jammed state at the end of the local sliding

$$\int_{w_1}^{w_2} F(w)dw = \frac{(F_{c2} - F_{c1})^2}{2k_U}. \tag{16}$$

From (13)–(15), that the force and stiffness are continuous at yield point 2, we have

$$F_{c2} = k_U w_{c2} \left[1 + 3\mathrm{NA}(w_{c2})^2\right] \tag{17}$$

$$b_2 k_U = k_U[1 + 3\mathrm{NA}(w_{c2})^2 + 6\mathrm{NA}(w_{c2})\mathrm{NA}'(w_{c2})w_{c2}]. \tag{18}$$

By substituting (17) and (18) into the first-order derivative of (16)

$$k_U w_{c2} \left[1 + 3\mathrm{NA}(w_{c2})^2\right] = (k_U w_{c2} \left[1 + 3\mathrm{NA}(w_{c2})^2\right] - F_{c1})$$

$$(1 + 3\mathrm{NA}(w_{c2})^2 + 6\mathrm{NA}(w_{c2})\mathrm{NA}'(w_{c2})w_{c2}) \tag{19}$$

we obtain

$$F_{c2} = \frac{b_2}{b_2 - 1} F_{c1} \tag{20}$$

where b_2 denotes that the stiffness of the structure in the fully sliding state is not strictly equivalent to that in its unjammed state but is close to the value of 1. By knowing the normalized distance NA(w) starts from the value of 1 and ends at 0, and also satisfies that the stiffness k is a monotonic decreasing function in the nonlinear regime, (13), (15), and (16) are solved by setting

$$\mathrm{NA}(w) = c + a_1 w^{-3/2} + a_2 w^{-1/2} + a_3 w^{1/2} F > F_{c1} \tag{21}$$

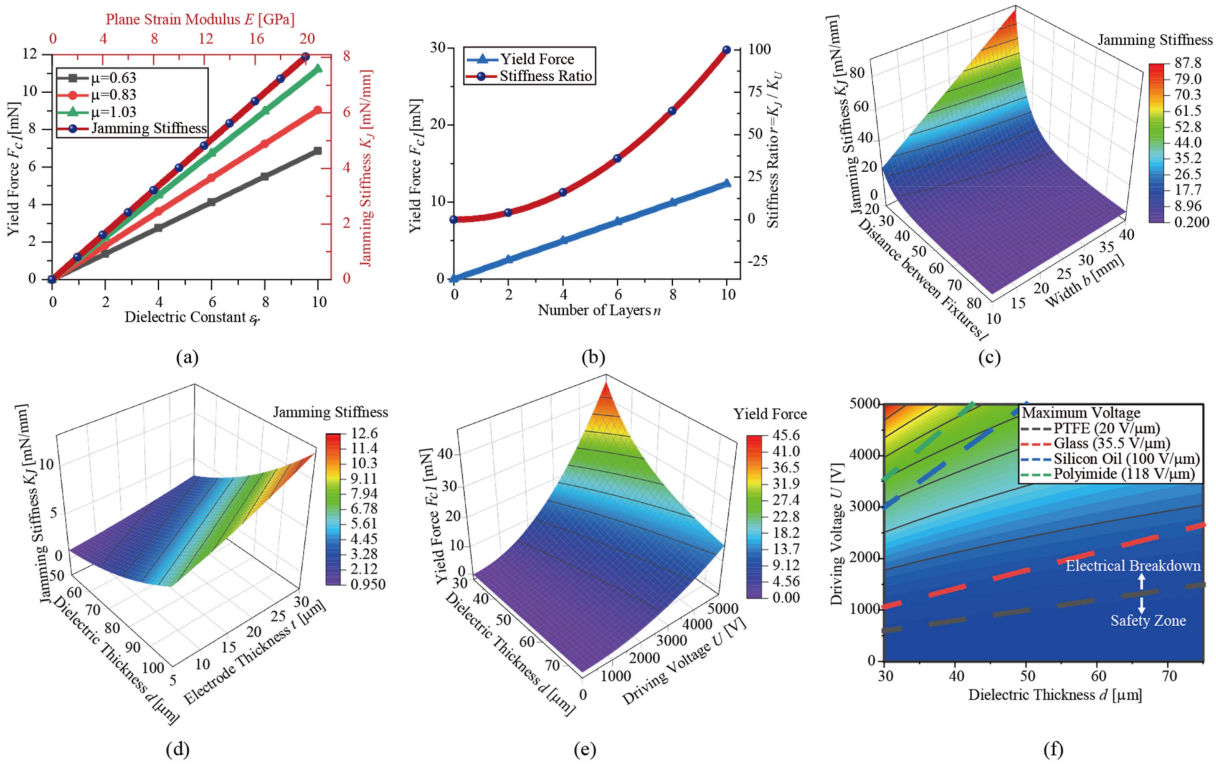

Fig. 3. Influences of design inputs on ELJS performances in terms of materials, geometry, and actuation. The effect of (a) material properties, regarding young's modulus, dielectric constant, and friction coefficient of an electrode film, and (b) geometries, such as the number of layers on the force of yield point 1 and the stiffness ratio, is analyzed. The influences of other geometrical dimensions, including (c) the distance between fixtures, width, (d) dielectric thickness, and electrode thickness (noted that $h = d + t$) on the jamming stiffness, are also analyzed. (e) Presents the driving voltage and dielectric thickness's influences on the force of yield point 1, followed by its (f) contour plot with bold dashed lines indicating common dielectric materials with different breakdown fields, revealing the relationship between dielectric thickness and maximum driving voltage. If not mentioned, other parameters are the same as the fabricated two-layer ELJS in this work.

where c, a_1, a_2, and a_3 are undetermined coefficients. The changing location of NA influences the stiffness of ELJS according to (7) or (14). The results and analysis are in the following section.

C. Parametrical Analysis

Based on the aforementioned model, the impact of parameters regarding materials, geometry, and actuation, on its stiffness-related performances is analyzed, as shown in Fig. 3(a)–(f). In the fully composite mode, the jamming stiffness becomes higher when plane strain modulus of electrode film [see Fig. 3(a)], the width [see Fig. 3(c)], the dielectric thickness, or the electrode thickness [see Fig. 3(d)] increases, or when the distance between fixtures decreases [see Fig. 3(c)]. The stiffness ratio is in a quadratic relationship with the number of layers, as shown in Fig. 3(b). The yield force of the fully composite mode rises for the higher dielectric constant, coefficient of friction, the number of layers, driving voltage, and the smaller dielectric thickness [see Fig. 3(a), (b), and (e)], while the electrode length has no impact on the yield force. The dielectric thickness and the breakdown strength of certain dielectric materials limit its maximum driving voltage. As shown in Fig. 3(f), if not considering the difference in breakdown strength, the maximum yield force increases with the dielectric thickness as the allowed driving voltage is higher. Similarly, dielectric materials with a higher breakdown strength own a stronger yielding force since the maximum driving voltage is higher with the same dielectric thickness. The unjamming stiffness and force of yield point 2 are not discussed here since they can be obtained by (6) and (20), respectively.

We also analyze the bending performance of the jamming structure in the nonlinear regime. As shown in Fig. 4(a), without voltage, the value of the stiffness ratio is 1 as a reference, while by the voltage supplied, it remains at a higher value of four at first, and then plummets when the deflection surpasses 0.5 mm ($l =$ 30 mm) and approaches 1. The larger distance between fixtures [see Fig. 4(a)] and smaller dielectric thickness [see Fig. 4(c)] prolong the fully composite regime and decelerate the change of the stiffness ratio during the nonlinear regime, while the width [see Fig. 4(b)] has no influence and the electrode thickness [see Fig. 4(d)] has little influence on them.

This parametric analysis is beneficial for structural improvement for satisfying different application scenarios. For instance, appropriate dimension adjustment is feasible for ELJS with high stiffness and high yield points. One approach would be increasing the width b, but the size of the structure is usually limited due to space constraints in practical applications. Another possible and direct solution is increasing the number of layers n. However, it will cause a decrease in the corresponding deflection of yield point 1 w_1. Thus, the required deflection

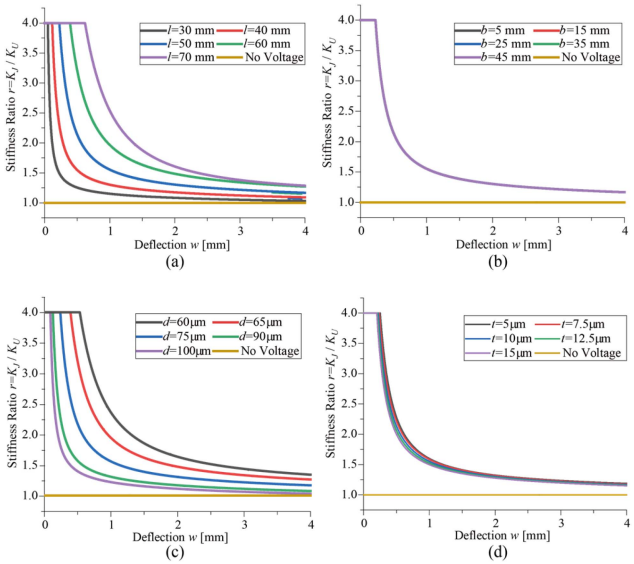

Fig. 4. Bending performance of ELJS. The impact of (a) the distance between two fixtures, (b) width, (c) dielectric thickness, and (d) electrode thickness on the stiffness ratio through the whole bending process, including linear behavior and nonlinear behavior. If not mentioned, other parameters are the same as the fabricated two-layer ELJS in this work.

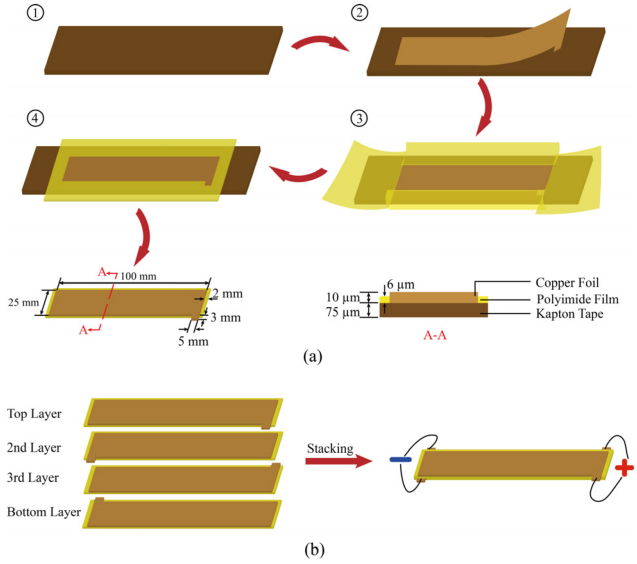

Fig. 5. Fabrication process of ELJS. (a) Electrode film is fabricated by a piece of copper foil pasting onto the Kapton tape substrate, and a PI film framing around the copper foil to prevent voltage breakdown. (b) Assembly method of a multilayer ELJS.

should be determined by specific application scenarios. The increase in driving voltage U, dielectric constant ε_r, and friction coefficient μ can compensate for the deflection since the yield force is elevated with the stiffness remaining still. However, the range of voltage U is limited by dielectric thickness d. Therefore, in terms of materials, dielectric with high dielectric strength and high dielectric constant ε_r is desired for stiffness performance improvement.

D. Materials and Fabrication of ELJS

An ELJS consists of multiple electrode films. These films are the same in structure. The fabrication process (see Fig. 5) is as follows.

1) At first, a piece of Kapton tape (DuPont, 75 μm) was fixed on a flat surface.
2) A piece of copper foil (100 mm $\times$ 25 mm, Wah Wei, 10 μm) was bonded to the tape substrate.
3) The edges of the copper foil were covered by polyimide (PI) films (DuPont, 10 μm) to prevent potential breakdown at the edges.
4) A section of the film was cut off, and a 5 mm $\times$ 3 mm narrow strip was reserved for an external wire connection to create a better adhesion condition [see Fig. 5(a)].
5) Finally, the ELJS was built by stacking multiple electrode films [see Fig. 5(b)]. The terminal strip of each film was intentionally located differently to avoid wire interference (which might lead to short circuits and structural failure during actuation).

Each electrode film weighs 0.51 g and measures 104 mm $\times$ 30 mm $\times$ 85 μm, PI frame and strips included. A two-layer ELJS can be only 170 μm thick.

III. Experiments and Results

A. Experiment Protocol

A two-layer and a four-layer ELJS under different driving voltages were tested in three-point bending tests, each test was repeated three times. The experimental setup is shown in Fig. 6(a). The ELJS was simply supported by two fixtures with a distance of 50 mm. A 3D-printed photopolymer anvil was mounted at the moving stage of a universal tensile testing machine (ZQ-990b, Zhiqu Precision Instruments). This anvil approached the midspan of the structure at a constant velocity of 2 mm/min and applied the concentrated external pressing load to the ELJS during the test. The pressing force was acquired by a force sensor (LSB 200, Futek Advanced Sensor Technology Inc.) installed at the end of the anvil connected to a DAQ board (TB-4330, National Instruments). The deflection of the ELJS was acquired by the tensile testing machine. A high-voltage function generator (Model 615-3, Trek Inc.) supplied driving voltage to the electrodes of ELJS. The transient response of the ELJS was measured by the same setup. A two-layer ELJS was pressed at the midspan by the anvil with 1 mm/min velocity. In the beginning, the voltage generator was off. Then, at a certain moment, the electrodes were supplied with a high voltage (3 kV), and the pressing force during this process (from the soft state to the rigid state) was recorded. The sampling frequency was 500 Hz. Similarly, the transient response of the ELJS from the rigid state to the soft state was also tested.

B. Variable Stiffness

Fig. 6(b) is the theoretical predictions and the experimental validation of a two-layer ELJS, demonstrating high accuracy. Young's modulus of the electrode film (7.736 GPa) was obtained

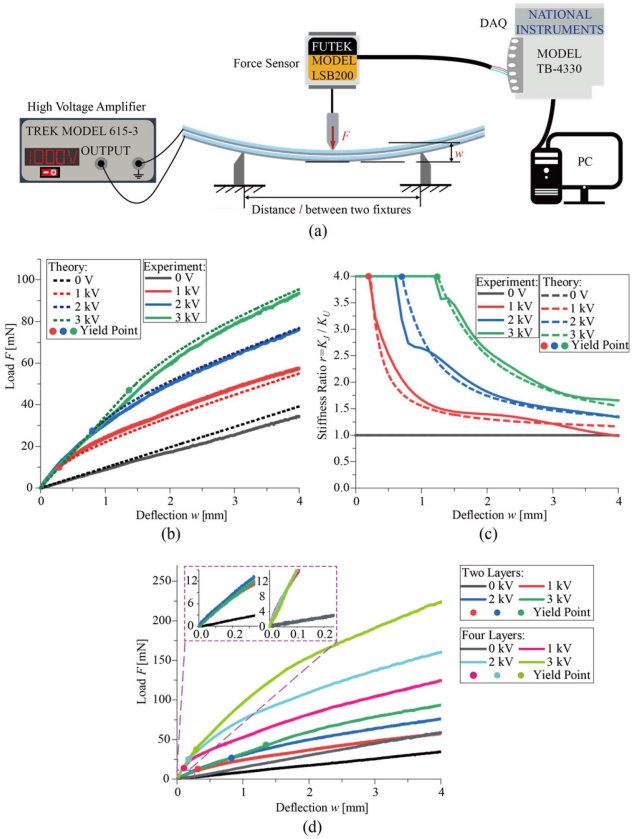

Fig. 6. Experimental results of ELJS. (a) Experimental setup of the three-point bending test. (b) Theoretical prediction and experimental validation data of a two-layer ELJS under 0–3 kV, and (c) its stiffness ratio. (d) Experimental data of a four-layer ELJS under 0–3 kV, the enlarged inset illustrates the stiffness variation between no applied voltage and kilovolts voltage applied.

by preliminary tensile tests in the prediction. The discrepancy between the experimental data (0 V) and estimation perhaps was induced by the slip between fixtures and the structure when a large deflection was caused (up to 4 mm). The value of k_U for all voltages is 0.88. The value of b_2 that acquired by trial, for 1 kV, 2 kV, and 3 kV are 1.14, 1.03, and 1.01, respectively. It is approaching the value of 1. The b_2 value of 1.14 can be attributed to a larger air gap under relatively low voltages, such as 1 kV. The solutions of NA(w), in the order of a_1, a_2, a_3, and c, are -0.04296, 0.5641, -0.02817, and 0.2267 for 1 kV, -0.2569, 1.0918, -0.0049, and 0.1378 for 2 kV, -0.6396, 1.5385, -0.0013, and 0.0829 for 3 kV. Fig. 6(c) reveals that the stiffness, in the beginning, is four times larger than that in the case without voltage driving, as predicted in (6) and Fig. 4. This relationship is not affected by the driving voltage. The $F-w$ curves for various driving voltages first exhibit the linear behavior (fully composite, high and constant stiffness), and then nonlinear behavior (local sliding, decreasing, and variable stiffness) appears as the load increases. The voltage rise increases the maximum static friction force, thus prolonging each regime (moving the yield points to further position, marked with solid circles in Fig. 6). The disagreements between the prediction and measurements in Fig. 6(b) and (c) can be

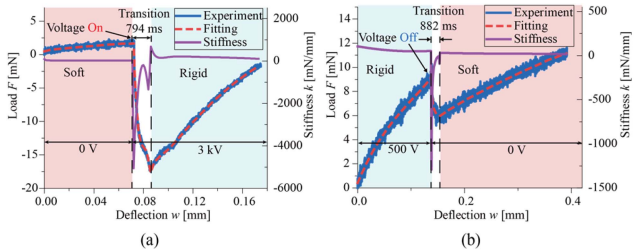

Fig. 7. Response time test of a two-layer ELJS from (a) soft state to rigid state and (b) from rigid state to soft state.

attributed to the pure friction and electrostatic adhesion model. Anomaly can be further reduced by introducing a more realistic stick-slip model between layers and an electrostatic adhesion model considering air gaps. Furthermore, the uncertainty of Young's modulus obtained by tensile tests can also contribute to the discrepancies.

Fig. 6(d) presents the experimental data of the four-layer ELJS, which shares a similar tendency with the two-layer structure and shows a stiffness 11 times larger than the one without voltage. Driven by the same voltage (e.g., 3 kV), the corresponding deflection of yield point 1 for the four-layer ELJS (0.3 mm) is approximately 1/4 times of that for the two-layer ELJS (1.2 mm), as predicted by (3), (5), and (10). A larger number of layers increases the stiffness ratio but decreases the deflection value of yield point 1, thus sacrificing the fully composite regime. Therefore, there is a tradeoff between the stiffness ratio and the fully composite regime when building a multilayer ELJS.

C. Response Time

As shown in Fig. 7(a), once the voltage was supplied, the stiffness increased. Theoretically, the ELJS becomes effective as soon as the electrodes are charged. According to the parallel plate capacitor model, the charging time 5τ ($\tau = RC$) is only 3.73 ns. This period is much smaller than the transition duration measured in this test (794 ms), perhaps because of the mechanical delay of the films, such as air gaps introduced by localized surface roughness [29], [30], [31]. The response time from the rigid state to the soft state is 882 ms [see Fig. 7(b)], a little longer than the period changing from the soft state to the rigid state. In summary, the transition of the stiffness variation is quick compared with other variable stiffness mechanisms. Such as fluid-driven mechanism [5], [6] depending on fluidic inflow/outflow, vacuum-driven mechanism [7], [11], [12] depending on vacuum pump inflow/outflow, and shape memory alloys [10] depending on thermal conditions, the transition time is commonly in seconds.

D. Power Consumption

The equivalent circuit of a two-layer ELJS is a capacitor in parallel with a resistor, as shown in Fig. 8(a). We measured the applied driving voltage and the corresponding current of the ELJS under 1 kV [see Fig. 8(b)] using an electrometer (Model 6514, Keithley Instruments). The current curve depicts

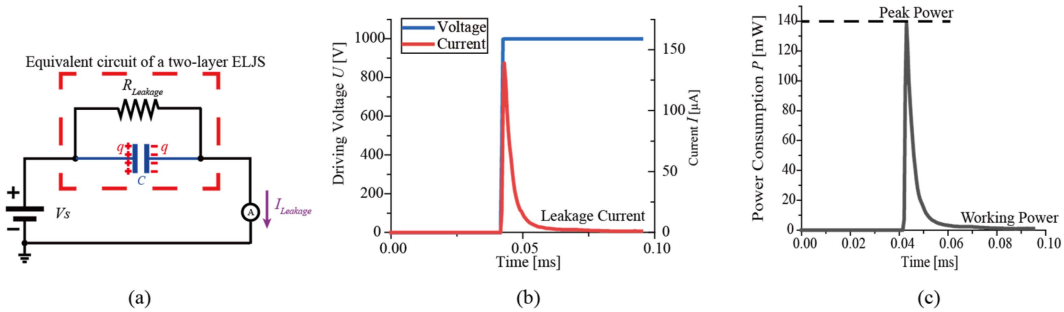

Fig. 8. Power consumption of a two-layer ELJS. (a) Schematic circuitry. (b) Driving voltage, charging current. (c) Power consumption of a two-layer ELJS.

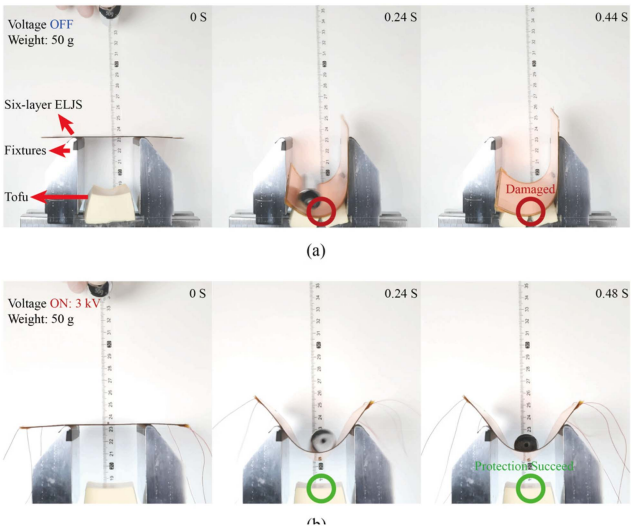

Fig. 9. Protection functionality. A six-layer ELJS (100 mm × 50 mm) is chronologically impacted by a 50 g weight (a) when no voltage is applied and damages the tofu beneath it, and (b) when 3 kV is applied and successfully protects the tofu. All weights are released from 10 cm height from the structure.

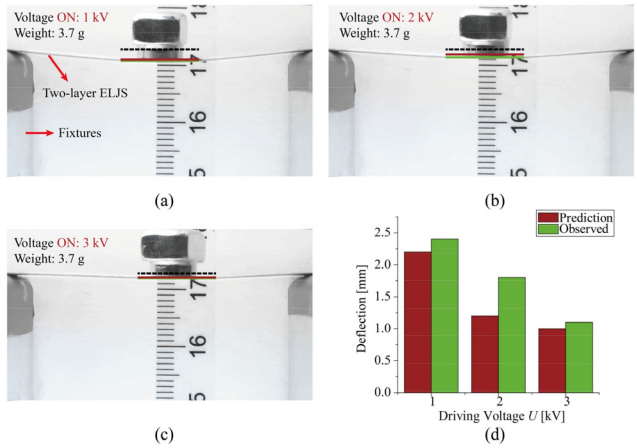

Fig. 10. Deflection prediction. A two-layer ELJS (100 mm × 25 mm) is loaded by a 3.7 g weight, causing different deflections under (a) 1 kV, (b) 2 kV, and (c) 3 kV. The dashed lines, solid green lines, and solid red lines indicate the initial positions (no weight applied), the observed positions, and the predicted positions of the structure, respectively. (d) Comparison between predicted and observed deflection values under different driving voltages.

the charging process of the structure. It drastically reaches its peak value (139 μA) right after the voltage is applied and gradually drops to the leakage current of 1 μA within 45 ns. The power consumption, as shown in Fig. 8(c), is calculated by $P = UI$. The instantaneous peak power of the ELJS device is 139 mW, which only takes place once the current reaches its maximum. The working power consumption is only 1 mW and remains stable after the charging process ends.

IV. Demonstration

First, a two-layer ELJS (100 mm × 50 mm) was fabricated. It successfully bore a 20 g weight under 1 kV, and then failed within one second once the voltage was off and slipped off from both ends of fixtures (S1), presenting a large range of stiffness variation and fast response. This function is useful for application scenarios where a fast and on-demand variable stiffness technique with simple control is needed, e.g., grippers for holding and releasing irregular objects. Another demonstration exhibits the capability of impact absorption (see Figs. 9 and S2). A six-layer ELJS of the same size was used here. A 50 g weight was released from a height of 10 cm, producing impacts on the structure. It failed to resist the impact, and the tofu placed beneath it was damaged [see Fig. 9(a)]. Under 3 kV, a 50 g weight was released from the same height. It was deflected but successfully kept the tofu intact [see Fig. 9(b)].

This functionality is applicable in damping, such as cushioning the landing process of a flying robot, where impact and damage might occur. At last, a 3.7 g weight was loaded to induce deflections of a two-layer structure (100 mm × 25 mm) under 1 kV, 2 kV, and 3 kV (Fig. 10(a)–(c) and S3). Deflections were recorded and compared with theoretical values, as shown in Fig. 10(d). The discrepancies might be caused by interlayer air gaps due to the roughness and flatness of electrode films. A stick-slip friction model can also be introduced for more accurate prediction.

V. Conclusion

This work builds a comprehensive model for the laminar jamming variable stiffness technique driven by electrostatic adhesion. This model is adequate to analyze and predict the linear and nonlinear regions of ELJS. The dependencies of

stiffness-related performances on design inputs were quantitatively analyzed, enabling the design process acceleration for determining the materials, geometry, and actuation to meet unique requirements. Three useful functions, on-demand fast variable stiffness, impact absorption, and accurate deflection prediction were demonstrated, illustrating how ELJS can endow new capabilities to the robotics community. For instance, soft grippers integrated with ELJS realize versatile grasping with variable stiffness functionality through direct voltage control and precise conformation to the irregular subjects with model prediction. For medical applications, an endoscope fabricated by ELJS as a force-exerting platform for end effectors is promising in minimally invasive surgery where a restricted workspace inside the human body requires accurate deflection for surgical manipulation to avoid unnecessary harm. Besides, scalable ELJS can be mounted on different sizes of fly robots to protect them from damage through energy absorption when landing or bumping.

Future work will focus on safety concerns (high driving voltage and dielectric insulation) and integrations of ELJS with soft robotics. A more extensive model can be established by developing a more general electrostatic adhesion model considering air gaps, which is applicable for ELJS with different arrangements, such as the anode-cathode-cathode-anode arrangement, where two layers of different dielectrics with different thicknesses in series. Stick-slip friction model should be involved to further describe the interlayer mechanical behaviors during sliding, especially for interfaces with different materials. For a multilayer ELJS above two layers, the mechanical behavior can be obtained by solving each NA movement in the corresponding state.

REFERENCES

[1] B. Tondu and P. Lopez, "Modeling and control of McKibben artificial muscle robot actuators," *IEEE Control Syst. Mag.*, vol. 20, no. 2, pp. 15–38, Apr. 2000, doi: 10.1109/37.833638.

[2] L. Margheri, C. Laschi, and B. Mazzolai, "Soft robotic arm inspired by the octopus: I From biological functions to artificial requirements," *Bioinspiration Biomimetics*, vol. 7, no. 2, 2012, Art. no. 025004.

[3] V. Kumar, U. H. Ko, Y. Zhou, J. Hoque, G. Arya, and S. Varghese, "Microengineered materials with self-healing features for soft robotics," *Adv. Intell. Syst.*, vol. 3, no. 7, 2021, Art. no. 2100005.

[4] G. Li et al., "Self-powered soft robot in the mariana trench," *Nature*, vol. 591, no. 7848, pp. 66–71, 2021.

[5] A. Shiva et al., "Tendon-based stiffening for a pneumatically actuated soft manipulator," *IEEE Robot. Automat. Lett.*, vol. 1, no. 2, pp. 632–637, Jul. 2016.

[6] T. Doi, S. Wakimoto, K. Suzumori, and K. Mori, "Proposal of flexible robotic arm with thin McKibben actuators mimicking octopus arm structure," in *Proc. IEEE/RSJ Int. Conf. Intell. Robots Syst.*, 2016, pp. 5503–5508.

[7] T. Ranzani, M. Cianchetti, G. Gerboni, I. D. Falco, and A. Menciassi, "A soft modular manipulator for minimally invasive surgery: Design and characterization of a single module," *IEEE Trans. Robot.*, vol. 32, no. 1, pp. 187–200, Feb. 2016.

[8] A. Jiang et al., "Robotic granular jamming: Does the membrane matter?," *Soft Robot.*, vol. 1, no. 3, pp. 192–201, 2014.

[9] M. Z. Miskin and H. M. Jaeger, "Adapting granular materials through artificial evolution," *Nature Mater.*, vol. 12, no. 4, pp. 326–331, 2013.

[10] M. Henke and G. Gerlach, "On a high-potential variable-stiffness device," *Microsystem Technol.*, vol. 20, no. 4/5, pp. 599–606, 2014.

[11] Y. S. Narang, A. Degirmenci, J. J. Vlassak, and R. D. Howe, "Transforming the dynamic response of robotic structures and systems through laminar jamming," *IEEE Robot. Automat. Lett.*, vol. 3, no. 2, pp. 688–695, Apr. 2018.

[12] Y. S. Narang, J. J. Vlassak, and R. D. Howe, "Mechanically versatile soft machines through laminar jamming," *Adv. Funct. Mater.*, vol. 28, no. 17, 2018, Art. no. 1707136.

[13] H. Wang, A. Yamamoto, and T. Higuchi, "Electrostatic-motor-driven electroadhesive robot," in *Proc. IEEE/RSJ Int. Conf. Intell. Robots Syst.*, 2012, pp. 914–919.

[14] M. Taghavi, T. Helps, and J. Rossiter, "Electro-ribbon actuators and electro-origami robots," *Sci. Robot.*, vol. 3, no. 25, 2018, Art. no. eaau9795.

[15] S. D. de Rivaz, B. Goldberg, N. Doshi, K. Jayaram, J. Zhou, and R. J. Wood, "Inverted and vertical climbing of a quadrupedal microrobot using electroadhesion," *Sci. Robot.*, vol. 3, no. 25, 2018, Art. no. eaau3038.

[16] G. Gu, J. Zou, R. Zhao, X. Zhao, and X. Zhu, "Soft wall-climbing robots," *Sci. Robot.*, vol. 3, no. 25, 2018, Art. no. eaat2874.

[17] M. A. Graule et al., "Perching and takeoff of a robotic insect on overhangs using switchable electrostatic adhesion," *Science*, vol. 352, no. 6288, pp. 978–982, 2016.

[18] Y. Chen et al., "A biologically inspired, flapping-wing, hybrid aerial-aquatic microrobot," *Sci. Robot.*, vol. 2, no. 11, 2017, Art. no. eaao5619.

[19] V. Ramachandran, J. Shintake, and D. Floreano, "All-fabric wearable electroadhesive clutch," *Adv. Mater. Technol.*, vol. 4, no. 2, 2019, Art. no. 1800313.

[20] V. V. Hinchet, H. Shea, and O. Hilliges, "DextrES: Wearable haptic feedback for grasping in VR via a thin form-factor electrostatic brake," in *Proc. 31st Annu. ACM Symp. User Interface Softw. Technol.*, 2018, pp. 901–912.

[21] S. Diller, C. Majidi, and S. H. Collins, "A lightweight, low-power electroadhesive clutch and spring for exoskeleton actuation," in *Proc. IEEE Int. Conf. Robot. Automat.*, 2016, pp. 682–689.

[22] R. Hinchet and H. Shea, "High force density textile electrostatic clutch," *Adv. Mater. Technol.*, vol. 5, no. 4, 2020, Art. no. 1900895.

[23] H. Wang et al., "Biologically inspired electrostatic artificial muscles for insect-sized robots," *Int. J. Robot. Res.*, vol. 40, no. 6/7, pp. 895–922, 2021.

[24] T. Wang, J. Zhang, Y. Li, J. Hong, and M. Y. Wang, "Electrostatic layer jamming variable stiffness for soft robotics," *IEEE ASME Trans. Mechatron.*, vol. 24, no. 2, pp. 424–433, Apr. 2019.

[25] U. A. Girhammar and V. K. A. Gopu, "Composite beam-columns with interlayer slip—Exact analysis," *J. Struct. Eng.*, vol. 119, no. 4, pp. 1265–1282, 1993.

[26] Y. Shi, J. A. Rogers, C. Gao, and Y. Huang, "Multiple neutral axes in bending of a multiple-layer beam with extremely different elastic properties," *J. Appl. Mech.*, vol. 81, no. 11, 2014, Art. no. 114501.

[27] S. Li, Y. Su, and R. Li, "Splitting of the neutral mechanical plane depends on the length of the multilayer structure of flexible electronics," *Proc. Math. Phys. Eng. Sci.*, vol. 472, no. 2190, 2016, Art. no. 20160087.

[28] S. Li, Y. Su, and R. Li, "Characterization of extensional multilayer microbeams in pull-in phenomenon and vibrations," *Proc. Math. Phys. Eng. Sci.*, vol. 472, no. 2190, 2016, Art. no. 20160087.

[29] Y. Wang, W. Lin, Z. Feng, and X. Li, "Electrostatic adhesion for added functionality of composite structures," *Int. J. Mech. Sci.*, vol. 54, no. 1, pp. 225–233, 2012.

[30] V. Alizadehyazdi, M. Bonthron, and M. Spenko, "An electrostatic/gecko-inspired adhesives soft robotic gripper," *IEEE Robot. Automat. Lett.*, vol. 5, no. 3, pp. 4679–4686, Jul. 2020.

[31] M. Dadkhah, D. Ruffatto III, Z. Zhao, and M. Spenko, "Increasing adhesion via a new electrode design and improved manufacturing in electrostatic/microstructured adhesives," *J. Electrostatics*, vol. 91, pp. 48–55, 2018.

[32] F. Caruso, G. Mantriota, L. Afferrante, and G. Reina., "A theoretical model for multilayer jamming systems," *Mech. Mach. Theory*, vol. 172, 2022, Art. no. 104788.

Cheng Chen received the B.S. degree in mechanical engineering from the University of Electronic Science and Technology of China, Chengdu, China, in 2019. He is currently working toward the Ph.D. degree in mechanical engineering with the Department of Mechanical and Energy Engineering, Southern University of Science and Technology, Shenzhen, China, and in biomedical engineering with the Department of Biomedical Engineering, National University of Singapore, Singapore, with Prof. H. Wang and Prof. H. Ren, respectively.

His research interests include soft robotics and variable stiffness.

Dongliang Fan received the B.S. degree in materials science and engineering from East China University of Science and Technology, Shanghai, China, in 2017 and the M.S. degree in polymer science and engineering from the University of Akron, Akron, OH, USA, in 2018. He is currently working toward the Ph.D. degree in mechanics with the Department of Mechanical and Energy Engineering, Southern University of Science and Technology, Shenzhen, China, with Prof. H. Wang.

His research interests include soft robotics and wearable sensors.

Hongliang Ren (Senior Member, IEEE) received the Ph.D. degree in electronic engineering (*specialized in biomedical engineering*) from The Chinese University of Hong Kong (CUHK), Hong Kong, in 2008.

He has navigated his academic journey through CUHK, Johns Hopkins University, Children's Hospital Boston, Harvard Medical School, Children's National Medical Center, USA, and National University of Singapore (NUS). He is currently an Associate Professor with the Department of Electronic Engineering, CUHK, and an Adjunct Associate Professor with the Department of Biomedical Engineering, NUS. His research interests include biorobotics, intelligent control, medical mechatronics, soft continuum robots, soft sensors, and multisensory learning in medical robotics.

Dr. Ren was a recipient of the NUS Young Investigator Award, the Engineering Young Researcher Award, the IAMBE Early Career Award 2018, the Interstellar Early Career Investigator Award 2018, and the ICBHI Young Investigator Award 2019. He is an Associate Editor for IEEE TRANSACTIONS ON AUTOMATION SCIENCE AND ENGINEERING and Medical and Biological Engineering and Computing.

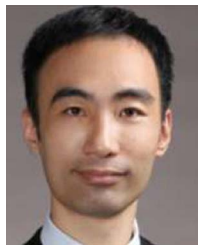

Hongqiang Wang (Senior Member, IEEE) received the B.S. and M.S. degrees in mechanical engineering from the Xi'an Jiao Tong University, Xi'an, China, in 2008 and 2011, respectively, and the Ph.D. degree in precision mechanical engineering from the Tokyo University, Tokyo, Japan, in 2015.

He is currently an Associate Professor with the Department of Mechanical and Energy Engineering, Southern University of Science and Technology, Shenzhen, China. His research interests include novel actuators, miniature robotics, new flexible actuators, soft robotics, and medical robotics.